

Fast non-destructive cavity readout of single atoms within a coherent atom array

Emma Deist,^{1,2,*} Yue-Hui Lu,^{1,2,*} Jacquelyn Ho,^{1,2} Mary Kate Pasha,^{1,2}
Johannes Zeiher,^{1,3,4} Zhenjie Yan,^{1,2} and Dan M. Stamper-Kurn^{1,2,5,†}

¹*Department of Physics, University of California, Berkeley, California 94720*

²*Challenge Institute for Quantum Computation, University of California, Berkeley, California 94720*

³*Max-Planck-Institut für Quantenoptik, 85748 Garching, Germany*

⁴*Munich Center for Quantum Science and Technology (MCQST), 80799 Munich, Germany*

⁵*Materials Sciences Division, Lawrence Berkeley National Laboratory, Berkeley, California 94720*

(Dated: 30th May 2022)

The non-destructive measurement of a subsystem within a larger quantum system is crucial for error correction during quantum computation, simulation, and metrology, and for studying open quantum system dynamics. In many quantum technologies based on trapped atoms, measurement is performed by imaging all atoms simultaneously, a process that is typically slow and that decoheres the entire quantum system. Here, we use a strongly coupled optical cavity to read out the state of a single tweezer-trapped ⁸⁷Rb atom within a small tweezer array. Measuring either atomic fluorescence or the transmission of light through the cavity, we detect both the presence and the state of an atom in the tweezer, requiring only tens of microseconds for state-selective detection, with state preparation and measurement infidelities of roughly 0.5% and atom loss probabilities of around 1%. Using a two-tweezer system, we find measurement on one atom within the cavity causes no observable hyperfine-state decoherence on a second atom located tens of microns from the cavity volume.

Numerous applications of controlled many-body quantum systems require that part of the system be measured while other parts remain coherent. Examples include error correction in quantum computation [1, 2], measurement-based quantum computation [3], quantum-error-corrected metrology [4–6], and an entanglement phase transition induced by measurements on an interacting quantum system [7, 8].

Achieving such subsystem-selective measurement is a challenge in several platforms for engineering large-scale quantum systems. For example, in many atom-based systems such as atom-tweezer arrays [9, 10], lattice-trapped atoms [11, 12], and trapped ion chains [13], the many-atom state is read out through optical fluorescence imaging. Given the practical limitations on the numerical aperture (NA) of imaging systems, an atom is detected only after it scatters very many photons, posing three significant drawbacks. First, the time required for high-fidelity fluorescence detection can be long, e.g. on the order of 10 [14–18] or 100 ms [19] in atomic tweezer arrays and quantum gas microscopes, respectively [20]. This duration can exceed the atomic coherence time, and also limits the repetition rate of experiments. Second, photons fluoresced by one atom can induce decoherence in neighboring atoms, precluding subsystem-selective measurement. Third, while scattering many photons, an atom may also undergo spontaneous Raman transitions, introducing infidelity into measurements of its internal state.

Here, we demonstrate local optical detection of an atomic tweezer array wherein the detected subsystem is measured with high fidelity while the undetected subsystem retains quantum coherence. For this, we use a strongly coupled cavity to detect a single optical

tweezer, allowing for rapid, state-sensitive, high-fidelity, low-atom-loss local measurement with minimal photon scattering of about 100 photons. We benchmark our measurement with a two-atom tweezer array, measuring single atoms sequentially by translating each tweezer trap into the cavity mode, and then detecting light emitted by the cavity that is either fluoresced by the driven atom or transmitted through the driven cavity [Fig. 1(a)]. We observe that an initially prepared hyperfine spin coherence of one atom persists even as the other atom is measured at high fidelity.

Our experimental setup is described in Ref. [21]. Briefly, a bulk optically trapped gas of ultracold ⁸⁷Rb atoms is prepared near the volume of a horizontal-axis, near-concentric in-vacuum Fabry-Pérot optical cavity with a mirror spacing of 9.4 mm. Atoms are loaded into optical tweezer traps formed by 808-nm-wavelength light that is projected vertically through a high-NA imaging system. An acousto-optical deflector (AOD) allows us to generate multiple traps in a one-dimensional array and to translate them perpendicularly to the cavity axis. We illuminate the tweezers with counter-propagating light that is detuned about $2\pi \times 35$ MHz below the D_2 $F = 2 \rightarrow F' = 3$ laser-cooling transition, and also with repump light, resonant with the $F = 1 \rightarrow F' = 2$ transition, both at a wavelength of 780 nm. This illumination reduces the population in each tweezer to either zero (empty tweezer) or one atom, which we distinguish by imaging the resulting fluorescence through the high-NA objective.

Single tweezer-trapped atoms can serve as long-lived qubits by encoding quantum information in the ground-state hyperfine spin [22, 23]. Following this approach, we prepare our atoms into the $F = 1$ or $F = 2$ manifold

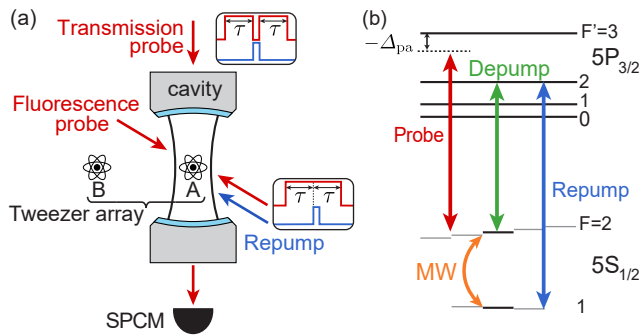


Figure 1. **Experiment schematic.** (a) Single atoms are loaded into each of two tweezers that can be translated perpendicularly to the cavity axis. Counter-propagating fluorescence probe beams, and also a unidirectional repump beam, are focused on the atom inside the cavity mode. The transmission probe beam couples directly into the cavity. (b) ^{87}Rb level structure. The probe beams (red) are detuned by Δ_{pa} from the $F = 2 \rightarrow F' = 3$ cycling transition. The repump and depump beams (blue and green) are on resonance with the $F = 1 \rightarrow F' = 2$ and $F = 2 \rightarrow F' = 2$ transitions. A resonant microwave pulse drives the Zeeman-insensitive $|F = 1, m_F = 0\rangle \rightarrow |F = 2, m_F = 0\rangle$ hyperfine transition.

by applying either depump ($F = 2 \rightarrow F' = 2$) or repump light, respectively [24] [Fig. 1(b)]. Combined with information from the aforementioned fluorescence image, the tweezers are thereby prepared in one of three tweezer states: empty, containing an atom in the $F = 1$ manifold, or containing an atom in the $F = 2$ manifold.

We use our cavity to measure a single tweezer, distinguishing each of these three tweezer states. The cavity reaches the single-atom strong coupling regime, with a cooperativity on the ^{87}Rb D_2 cycling transition of $C = g_0^2/(2\kappa\gamma) = 2.3$ with $\{g_0, \kappa, \gamma\} = 2\pi \times \{2.7, 0.53, 3.0\}$ MHz. Here, g_0 is the maximum atom-photon coupling strength between the $F = 2$ and $F' = 3$ stretched states at a field antinode in the center of the TEM_{00} cavity mode with a beam waist of $w_0 = 20(3) \mu\text{m}$. The half-linewidths of the cavity and atomic resonances are κ and γ , respectively.

Our high-cooperativity cavity supports two measurement methods. In the fluorescence method, we directly illuminate the atom and collect its fluorescence using the cavity. Strong atom-cavity coupling results in a large collection efficiency into a single optical mode that is detected with little background noise. In the transmission method, we drive the cavity near its resonance and measure the transmission of cavity probe light. Here, atom-cavity hybridization causes a single atom to broaden (at low C) or split (at high C) the cavity resonance line, reducing the transmitted intensity. Single-atom detection using strongly coupled cavities has been demonstrated previously, both through fluorescence [25, 26] and cavity transmission or reflection [25, 27, 28]. The present work extends these results to measurements on atoms trapped

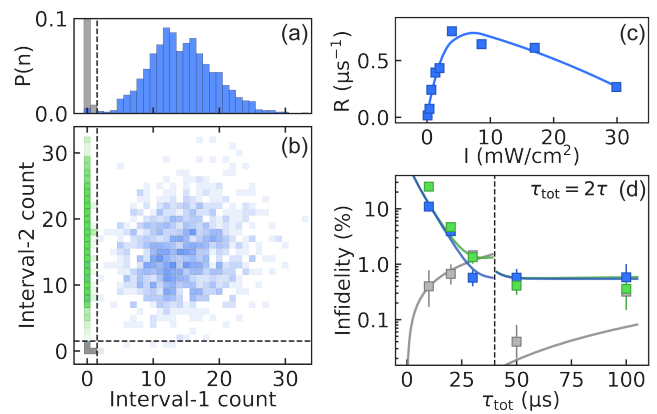


Figure 2. **Fluorescence measurement.** A single-probe histogram (a) and two-probe scatter plot (b) show the detected photon counts for tweezers in the no-atom (gray), $F = 2$ atom (blue), or $F = 1$ atom (green) state, taken with $\tau = 25 \mu\text{s}$ and $\Delta_{\text{pc}} = -2\pi \times 10$ MHz. The threshold (dashed line) between high and low fluorescence is set between 1 and 2 detected photons. (c) The optimal probe intensity I yields a maximum high count rate of $R = 0.76 \mu\text{s}^{-1}$. Solid line is a guide to the eye. (d) SPAM infidelity is determined for total measurement times $\tau_{\text{tot}} = 2\tau$ from 10 to $100 \mu\text{s}$. Solid lines are fits to a model described in [24]. For $\tau_{\text{tot}} \leq 40 \mu\text{s}$, indicated by the vertical gray line, both the data and model are calculated using a lower detection threshold between 0 and 1 photons.

and transported in configurable optical tweezers and advances the state-of-the-art with faster and higher-fidelity state-sensitive local measurements.

In both measurement methods, three-state sensitivity is achieved by probing the atom-cavity system in two consecutive probe intervals. In each interval of duration τ , using probe light near the $F = 2 \rightarrow F' = 3$ transition, we determine whether the cavity contains a single atom in the $F = 2$ manifold. This is done by counting photons emitted from the cavity using a single-photon counting module (SPCM) with a total quantum efficiency of $\eta = 0.25$ [24]. The detection path and SPCM are polarization-insensitive. A positive detection of an $F = 2$ atom is indicated by the observed photon number being either higher [fluorescence, see Fig. 2(a)] or lower [transmission, see Fig. 3(a)] than an optimized threshold. The second probe interval begins with (for fluorescence) or is preceded by (for transmission) local illumination of the detected tweezer with repump light for $\tau_{\text{rp}} = 5 \mu\text{s}$, driving an atom in the $F = 1$ manifold to the $F = 2$ manifold [see Fig. 1(a) insets]. The negative detection of an $F = 2$ atom in the first interval followed by a positive detection in the second interval measures the tweezer as containing an $F = 1$ atom, whereas a negative detection in both intervals measures the tweezer as being empty.

In the cavity fluorescence method, we set the cavity resonance frequency ω_c to be detuned by $\Delta_{\text{ca}} = \omega_c - \omega_a = -2\pi \times 10$ MHz below the laser-cooling transition frequency ω_a . We illuminate the atom with ver-

tically counter-propagating probe beams in a lin-perp-lin configuration in order to provide polarization gradient cooling during measurements. The probe frequency ω_p is slightly below that of the cavity resonance, with detuning $\Delta_{pc} = \omega_p - \omega_c \sim -\kappa/2$ so that the atomic motion is further cooled by cavity backaction [29]. The probe light intensity is set to maximize the photodetection rate $R = R_{\max}$ of a $F = 2$ tweezed atom in the cavity [Fig. 2(c)]a; lower probe intensity drives the atom below saturation, whereas higher probe intensity shifts the incoherent fluorescence spectrum outside the bandwidth of the cavity [30, 31]. Experimentally, we find $R_{\max} \simeq 0.76 \mu\text{s}^{-1}$, which is below the theoretical maximum of $R_0 = \eta g_0^2 / (4\kappa) = 5.4 \mu\text{s}^{-1}$ predicted for a two-level atom [24]. This difference may be explained by two effects. First, the tweezer-trapped atom is poorly localized along the cavity axis, exhibiting rms position fluctuations of up to 200 nm with respect to the standing-wave pattern (periodicity of 390 nm) of the cavity mode; see Ref. [21]. The effective square of the atom-cavity coupling strength is thus averaged roughly to $g_{\text{eff}}^2 \simeq g_0^2/2$ owing to spatial random sampling. Second, internal state dynamics induced by the probe light drives the atom between Zeeman sublevels of the ground and excited states, reducing the effective time-averaged coupling to the two polarization modes supported by the cavity. We estimate this effect reduces the maximum cavity emission rate by an additional factor of 0.28 [24].

Fluorescence measurement outcomes, obtained after preparing a single intracavity tweezer in each of the three tweezer states, are shown in Fig. 2. For a probe interval of $\tau = 25 \mu\text{s}$, we observe a large contrast between the photon number detected for a tweezer prepared in the $F = 2$ state, and that detected for either the no-atom or $F = 1$ states [Fig. 2(a)]. Combining data from two consecutive $25 \mu\text{s}$ probe intervals (total measurement time of $\tau_{\text{tot}} = 2\tau = 50 \mu\text{s}$), and setting the threshold for state detection between 1 and 2 photons, we achieve a state preparation and measurement (SPAM) error of several times 10^{-3} for each of the three initial tweezer states (Table I). For shorter τ [Fig. 2(d)], statistical fluctuations in the detected photon number lead us to misidentify bright states as dark states in either the first or second probe intervals, leading to infidelity in $F = 2$ and $F = 1$ state detection, respectively. For longer τ , state preparation error and false detection error caused by the depumping of an $F = 2$ atom before detecting an above-threshold number of photons set a limit on the achievable fidelity. We estimate that these two error sources contribute roughly equally to the overall SPAM error [24]. Table I also reports low atom loss probabilities on the order of 1%, with higher loss rates for atoms in the $F = 2$ manifold due to scattering-induced heating through both probe intervals.

In the cavity transmission method, we drive the cavity with light that is resonant with both the cavity and the atom ($\Delta_{ca} = \Delta_{pc} = 0$). The circularly polarized

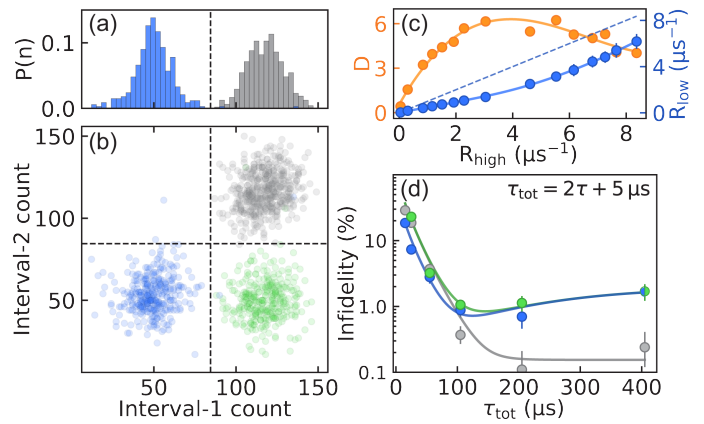


Figure 3. **Transmission measurement.** A single-probe histogram (a) and two-probe scatter plot (b) show the detected photon counts for tweezers in the no-atom (gray), $F = 2$ atom (blue), or $F = 1$ atom (green) state, taken with $\tau = 50 \mu\text{s}$ and $\Delta_{pc} = 0$. The threshold (dashed line) between high and low transmission is set above 77 detected photons. (c) The transmitted photon count rate with an $F = 2$ atom in the cavity (R_{low} , blue) is lower than the rate (R_{high} , x axis and dotted line) observed without. Ashman’s D (orange), a measure of the separation between R_{low} and R_{high} , reaches a maximum owing to atomic saturation. Lines are guides to the eye. (d) SPAM infidelity is determined for each of the initial tweezer states, with total measurement times $\tau_{\text{tot}} = 2\tau + 5 \mu\text{s}$ ranging from 15 to 205 μs . The threshold between high and low is selected to minimize infidelity at each τ . Lines are fits to a model described in [24].

probe light, together with a weak magnetic field applied along the cavity axis, pumps $F = 2$ atoms into the spin-stretched state, maximizing their coupling to the cavity. For weak probe light, we observe that an $F = 2$ atom in the cavity reduces the detected transmitted photon rate R_{low} to 0.4 times the rate R_{high} observed with either no atoms or an $F = 1$ atom in the cavity. The theoretical prediction in the low-saturation regime gives $R_{\text{low}}/R_{\text{high}} = (1 + 2C)^{-2}$ for fixed atom-cavity coupling strength. Averaging over a uniform atomic spatial distribution along the cavity axis yields $R_{\text{low}}/R_{\text{high}} = 0.27$ for our system.” The difference between the observed and expected transmission reduction may be explained by an inhomogeneous broadening of the atomic resonance

Table I. Measurement infidelity and loss probability

		No atom	F=1	F=2
Fluorescence $2 \times (\tau = 25 \mu\text{s})$	Outcome	low-low	low-high	high-X
	Infidelity	0.04(3) %	0.4(2) %	0.6(2) %
	Loss prob.	n/a	0.2(2) %	1.4(3) %
Transmission $2 \times (\tau = 50 \mu\text{s})$ $+ 5 \mu\text{s}$	Outcome	high-high	high-low	low-X
	Infidelity	0.4(1) %	1.1(2) %	0.9(2) %
	Loss prob.	n/a	0.7(3) %	1.4(2) %

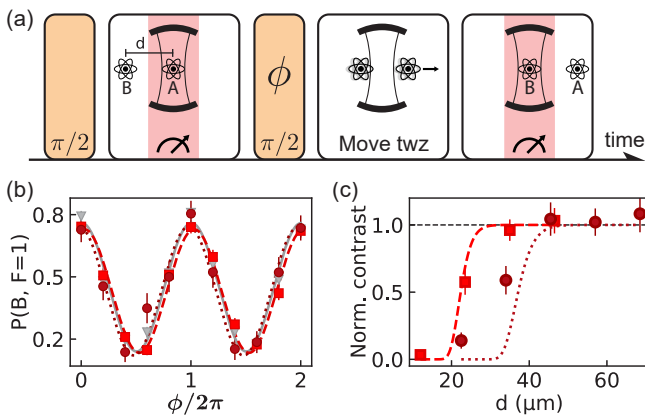


Figure 4. **Local measurement.** (a) Ramsey sequence schematic. Atom A (B) is initially located inside (outside) the cavity. Both are prepared in a two-hyperfine-state superposition using a microwave $\pi/2$ pulse. Atom A is measured with a total measurement duration τ_{tot} , both tweezers are repositioned within $200 \mu\text{s}$, and then atom B is measured. (b) The $F = 1, m_F = 1$ state probability of atom B, $P(B, F = 1)$, shows Ramsey fringes as the phase ϕ of the second pulse is varied. We observe no distinction between Ramsey fringes measured following fluorescence (light red squares, $\tau = 25 \mu\text{s}$) and transmission (dark red circles, $\tau = 50 \mu\text{s}$) detections of atom A, and no detection of atom A (gray). Normalized contrast is defined as the ratio of the Ramsey fringe contrasts observed with and without an atom A measurement. (c) Normalized contrast vs. the initial distance of atom B from the cavity center, with τ settings as in (b).

of roughly 4 MHz, caused by the ac Stark shift of the tweezer trap light [25]. At high probe intensity, atomic saturation leads to $R_{\text{high}} - R_{\text{low}}$ reaching a constant difference of roughly $2.4 \mu\text{s}^{-1}$. At an intermediate probe intensity setting of $R_{\text{high}} \simeq 2.2 \mu\text{s}^{-1}$, the bimodal separation statistic D [32] between the high and low photon count distributions reaches its maximum [Fig. 3(c)].

Transmission measurements made at this optimal probe intensity, with two probe intervals of $\tau = 50 \mu\text{s}$ each ($\tau_{\text{tot}} = 2\tau + 5 \mu\text{s} = 105 \mu\text{s}$), again show clear distinctions among tweezers prepared initially in each of the three tweezer states [Fig. 3(a)]. The detection infidelities and atom loss (Table I) are comparable to those obtained through fluorescence. However, the smaller contrast between high and low detection rates causes the transmission method to be generically slower than the fluorescence method of detection. Transmission measurements with a higher C would be interaction-free [33], thus suppressing depumping errors and mechanical effects from light scattering, which provides particular advantages for detecting trapped particles, such as single molecules [34, 35], that lack a cycling optical transition.

Next, we demonstrate that our cavity-enhanced detection is not only fast and high-fidelity, but also local. For this, we perform a Ramsey sequence on a two-atom tweezer system, where atom A is initially trapped within

the cavity and atom B is trapped at a variable radial distance d outside the cavity. We prepare the atoms in a coherent two-hyperfine-state superposition by optically pumping both atoms into the $|F = 2, m_F = 0\rangle$ state, and then applying a global microwave $\pi/2$ pulse coupling to the $|F = 1, m_F = 0\rangle$ state [24]. A subsystem measurement is performed by detecting the state of atom A, using either detection method with optimal probe times in Table I. The coherence of atom B is then probed by applying a second $\pi/2$ pulse with a variable phase offset ϕ to complete the Ramsey sequence; translating atom B into and atom A out of the cavity simultaneously within $200 \mu\text{s}$; and performing a cavity measurement of atom B [see Fig. 4(a)].

Measurements on atom B show a characteristic Ramsey fringe as ϕ is varied [Fig. 4(b)]. The limited fringe contrast of about 0.6 observed even without detecting atom A arises from imperfect preparation in the $m_F = 0$ magnetic sublevel and ac Stark shifts of the microwave frequency by tweezer light. To quantify additional loss of coherence caused by subsystem measurement, we determine a normalized contrast, taking the ratio of the fringe contrasts observed with and without an intermediate measurement of atom A.

We observe a normalized Ramsey contrast above 97% on atom B after measurements performed on atom A with 84% confidence level [24], when atom B is $d = 34.5 \mu\text{m}$ ($d = 46.0 \mu\text{m}$) away from the cavity mode center for fluorescence (transmission) measurement. A fluorescence measurement of atom A begins to affect the coherence of atom B once atom B is within about $20 \mu\text{m}$ of the cavity center [36]. This length scale is consistent with the beam waists of the fluorescence probe beams [24]. A transmission measurement begins to affect atom B at a larger distance of roughly $35 \mu\text{m}$ from the cavity center, consistent with the beam waist of the cavity mode [21].

The integration of cavity-enhanced measurement with atomic tweezer arrays offers particular advantages to the development of the atom and molecule tweezer platform for quantum science. In this work, we achieve measurement infidelities comparable to the best previous results in atomic tweezer systems [17], but in a manner that not only allows subsystem-selective measurement but also is much faster, with the measurement time being far shorter than the second-scale hyperfine-state coherence of tweezer-trapped atoms [37, 38]. The measurement time is even shorter than the $\sim 100 \mu\text{s}$ lifetime of the Rydberg states commonly used in Rydberg-tweezer systems [39]. Combined with the low probability of losing a trapped atom during detection, cavity-based measurement could also enable the deterministic preparation of atom arrays assembled atom-by-atom, without requiring free-space imaging and re-sorting [9, 10, 40–42].

The detection time, infidelity, and loss of our measurement could be reduced further by several experimental improvements. Increasing g_0 and κ simultan-

ously would allow for more efficient and faster detection of scattered photons. Better constraints on atomic motion, achieved by improved laser cooling or by stronger confinement along the cavity axis, would mitigate the effective motional reduction of atom-cavity coupling that we presently observe. Speed limits imposed by the need to transport atoms into the cavity prior to measurement could be improved by employing optical-lattice-based conveyors [43]. Transport could be eliminated altogether by maintaining the tweezer array entirely within the cavity volume and using rapid ac Stark shifts realized with local illumination to bring atoms selectively into resonance with the cavity for detection [18]. The atom loss probability could be reduced by using real-time processing and an adaptive measurement that stops each probe interval when a measurement outcome is obtained, and also by applying laser cooling briefly after detection.

We thank C. Liu for assistance in the lab and J. Gerber for comments on the manuscript. We acknowledge support from the AFOSR (Grant No. FA9550-19-10328), from ARO through the MURI program (Grant No. W911NF-20-1-0136), from DARPA (Grant No. W911NF2010090), and from the NSF QLCI program through grant number OMA-2016245. E.D. acknowledges support from the NSF Graduate Research Fellowship Program. J.H. acknowledges support from the NIH Molecular Biophysics Training Grant (Grant No. 5T32GM008295-31). J.Z. acknowledges support from the BMBF through the program “Quantum technologies - from basic research to market” (Grant No. 13N16265).

* These authors contributed equally to this work.

† dmsk@berkeley.edu

- [1] P. W. Shor, Scheme for reducing decoherence in quantum computer memory, *Phys. Rev. A* **52**, R2493 (1995).
- [2] A. M. Steane, Error Correcting Codes in Quantum Theory, *Phys. Rev. Lett.* **77**, 793 (1996).
- [3] R. Raussendorf and H. J. Briegel, A One-Way Quantum Computer, *Phys. Rev. Lett.* **86**, 5188 (2001).
- [4] E. M. Kessler, I. Lovchinsky, A. O. Sushkov, and M. D. Lukin, Quantum error correction for metrology, *Phys. Rev. Lett.* **112**, 150802 (2014).
- [5] W. Dür, M. Skotiniotis, F. Fröwis, and B. Kraus, Improved quantum metrology using quantum error correction, *Phys. Rev. Lett.* **112**, 080801 (2014).
- [6] S. Zhou and L. Jiang, Optimal approximate quantum error correction for quantum metrology, *Phys. Rev. Res.* **2**, 013235 (2020).
- [7] Y. Li, X. Chen, and M. P. A. Fisher, Quantum Zeno effect and the many-body entanglement transition, *Phys. Rev. B* **98**, 205136 (2018).
- [8] B. Skinner, J. Ruhman, and A. Nahum, Measurement-Induced Phase Transitions in the Dynamics of Entanglement, *Phys. Rev. X* **9**, 031009 (2019).
- [9] D. Barredo, S. D. Léséleuc, V. Lienhard, T. Lahaye, and A. Browaeys, An atom-by-atom assembler of defect-free arbitrary two-dimensional atomic arrays, *Science* **354**, 1021 (2016).
- [10] M. Endres, H. Bernien, A. Keesling, H. Levine, E. R. Anschuetz, A. Krajenbrink, C. Senko, V. Vuletić, M. Greiner, and M. D. Lukin, Atom-by-atom assembly of defect-free one-dimensional cold atom arrays, *Science* **354**, 1024 (2016).
- [11] Y. Wang, X. Zhang, T. A. Corcovilos, A. Kumar, and D. S. Weiss, Coherent addressing of individual neutral atoms in a 3d optical lattice, *Phys. Rev. Lett.* **115**, 043003 (2015).
- [12] C. Gross and I. Bloch, Quantum simulations with ultracold atoms in optical lattices, *Science* **357**, 995 (2017).
- [13] C. D. Bruzewicz, J. Chiaverini, R. McConnell, and J. M. Sage, Trapped-ion quantum computing: Progress and challenges, *Appl. Phys. Rev.* **6**, 021314 (2019).
- [14] A. Fuhrmanek, R. Bourgain, Y. R. P. Sortais, and A. Browaeys, Free-space lossless state detection of a single trapped atom, *Phys. Rev. Lett.* **106**, 133003 (2011).
- [15] M. Kwon, M. F. Ebert, T. G. Walker, and M. Saffman, Parallel low-loss measurement of multiple atomic qubits, *Phys. Rev. Lett.* **119**, 180504 (2017).
- [16] M. Martinez-Dorantes, W. Alt, J. Gallego, S. Ghosh, L. Ratschbacher, Y. Völzke, and D. Meschede, Fast nondestructive parallel readout of neutral atom registers in optical potentials, *Phys. Rev. Lett.* **119**, 180503 (2017).
- [17] J. P. Covey, I. S. Madjarov, A. Cooper, and M. Endres, 2000-times repeated imaging of strontium atoms in clock-magic tweezer arrays, *Phys. Rev. Lett.* **122**, 173201 (2019).
- [18] A. Urech, I. H. A. Knottnerus, R. J. C. Spreeuw, and F. Schreck, Narrow-line imaging of single strontium atoms in shallow optical tweezers, arXiv:2202.05727 (2022).
- [19] C. Gross and W. S. Bakr, Quantum gas microscopy for single atom and spin detection, *Nat. Phys.* **17**, 1316 (2021).
- [20] We note recent efforts that achieve fast free-space detection of tweezer-trapped neutral atoms through careful engineering of fluorescence detection [44] and Rydberg-ensemble-assisted imaging [45].
- [21] E. Deist, J. A. Gerber, Y.-H. Lu, J. Zeiher, and D. M. Stamper-Kurn, Superresolution microscopy of optical fields using tweezer-trapped single atoms, *Phys. Rev. Lett.* **128**, 083201 (2022).
- [22] T. Xia, M. Lichtman, K. Maller, A. Carr, M. Piotrowicz, L. Isenhower, and M. Saffman, Randomized Benchmarking of Single-Qubit Gates in a 2D Array of Neutral-Atom Qubits, *Phys. Rev. Lett.* **114**, 100503 (2015).
- [23] H. Levine, A. Keesling, G. Semeghini, A. Omran, T. T. Wang, S. Ebadi, H. Bernien, M. Greiner, V. Vuletić, H. Pichler, and M. D. Lukin, Parallel Implementation of High-Fidelity Multiqubit Gates with Neutral Atoms, *Phys. Rev. Lett.* **123**, 170503 (2019).
- [24] See Supplemental Material.
- [25] J. Bochmann, M. Mücke, C. Guhl, S. Ritter, G. Rempe, and D. L. Moehring, Lossless State Detection of Single Neutral Atoms, *Phys. Rev. Lett.* **104**, 203601 (2010).
- [26] J. Gallego, W. Alt, T. Macha, M. Martinez-Dorantes, D. Pandey, and D. Meschede, Strong Purcell Effect on a Neutral Atom Trapped in an Open Fiber Cavity, *Phys. Rev. Lett.* **121**, 173603 (2018).

- [27] R. Gehr, J. Volz, G. Dubois, T. Steinmetz, Y. Colombe, B. L. Lev, R. Long, J. Esteve, and J. Reichel, Cavity-Based Single Atom Preparation and High-Fidelity Hyperfine State Readout, *Phys. Rev. Lett.* **104**, 203602 (2010).
- [28] T. Dordevic, P. Samutpraphoot, P. L. Ocola, H. Bernien, B. Grinkemeyer, I. Dimitrova, V. Vuletić, and M. D. Lukin, Entanglement transport and a nanophotonic interface for atoms in optical tweezers, *Science* **373**, 1511 (2021).
- [29] S. Nuszmann, K. Murr, M. Hijlkema, B. Weber, A. Kuhn, and G. Rempe, Vacuum-stimulated cooling of single atoms in three dimensions, *Nat. Phys.* **1**, 122 (2005).
- [30] B. R. Mollow, Power spectrum of light scattered by two-level systems, *Phys. Rev.* **188**, 1969 (1969).
- [31] H. J. Kimble and L. Mandel, Theory of resonance fluorescence, *Phys. Rev. A* **13**, 2123 (1976).
- [32] Given two distributions with means $\mu_{1,2}$ and standard deviations $\sigma_{1,2}$, Ashman's D statistic for bimodal separation is defined as $D = |\mu_1 - \mu_2|/\sqrt{(\sigma_1^2 + \sigma_2^2)/2}$; see Ref. [46].
- [33] P. Kwiat, H. Weinfurter, T. Herzog, A. Zeilinger, and M. A. Kasevich, Interaction-Free Measurement, *Phys. Rev. Lett.* **74**, 4763 (1995).
- [34] L. Anderegg, L. W. Cheuk, Y. Bao, S. Burchesky, W. Ketterle, K.-K. Ni, and J. M. Doyle, An optical tweezer array of ultracold molecules, *Science* **365**, 1156 (2019), arXiv:1902.00497.
- [35] J. T. Zhang, L. R. B. Picard, W. B. Cairncross, K. Wang, Y. Yu, F. Fang, and K.-K. Ni, An optical tweezer array of ground-state polar molecules, *Quantum Sci. Technol.* **7**, 035006 (2022), arXiv:2112.00991.
- [36] Ref. [47] demonstrates fast local detection in a trapped ion platform, with low measurement-induced decoherence for ions with separations of hundreds of micrometers.
- [37] D. Bluvstein, H. Levine, G. Semeghini, T. T. Wang, S. Ebadi, M. Kalinowski, A. Keesling, N. Maskara, H. Pichler, M. Greiner, V. Vuletić, and M. D. Lukin, A quantum processor based on coherent transport of entangled atom arrays, *Nature* **604**, 451 (2022), arXiv:2112.03923.
- [38] M. A. Norcia, A. W. Young, W. J. Eckner, E. Oelker, J. Ye, and A. M. Kaufman, Seconds-scale coherence on an optical clock transition in a tweezer array, *Science* **366**, 93 (2019).
- [39] I. I. Beterov, I. I. Ryabtsev, D. B. Tretyakov, and V. M. Entin, Quasiclassical calculations of blackbody-radiation-induced depopulation rates and effective lifetimes of Rydberg nS, nP, and nD alkali-metal atoms with $n \leq 80$, *Phys. Rev. A* **79**, 1 (2009).
- [40] Y. Miroshnychenko, W. Alt, I. Dotsenko, L. Förster, M. Khudaverdyan, D. Meschede, D. Schrader, and A. Rauschenbeutel, An atom-sorting machine, *Nature* **442**, 151 (2006).
- [41] K. M. Fortier, S. Y. Kim, M. J. Gibbons, P. Ahmadi, and M. S. Chapman, Deterministic Loading of Individual Atoms to a High-Finesse Optical Cavity, *Phys. Rev. Lett.* **98**, 233601 (2007).
- [42] H. Kim, W. Lee, H.-g. Lee, H. Jo, Y. Song, and J. Ahn, In situ single-atom array synthesis using dynamic holographic optical tweezers, *Nat. Commun.* **7**, 13317 (2016).
- [43] S. Kuhr, W. Alt, D. Schrader, M. Müller, V. Gomer, and D. Meschede, Deterministic Delivery of a Single Atom, *Science* **293**, 278 (2001).
- [44] A. Bergschneider, V. M. Klinkhamer, J. H. Becher, R. Klemt, G. Zürn, P. M. Preiss, and S. Jochim, Spin-resolved single-atom imaging of li 6 in free space, *Phys. Rev. A* **97**, 063613 (2018).
- [45] W. Xu, A. V. Venkatramani, S. H. Cantú, T. Šumarac, V. Klüsener, M. D. Lukin, and V. Vuletić, Fast preparation and detection of a rydberg qubit using atomic ensembles, *Phys. Rev. Lett.* **127**, 050501 (2021).
- [46] K. A. Ashman, C. M. Bird, and S. E. Zepf, Detecting bimodality in astronomical datasets, *Astron. J.* **108**, 2348 (1994).
- [47] S. Crain, C. Cahall, G. Vrijnsen, E. E. Wollman, M. D. Shaw, V. B. Verma, S. W. Nam, and J. Kim, High-speed low-crosstalk detection of a 171Yb+ qubit using superconducting nanowire single photon detectors, *Commun. Phys.* **2**, 1 (2019).

Supplemental Material:

Fast non-destructive cavity readout of single atoms within a coherent atom array

Emma Deist,^{1,2,*} Yue-Hui Lu,^{1,2,*} Jacquelyn Ho,^{1,2} Mary Kate Pasha,^{1,2}
 Johannes Zeiher,^{1,3,4} Zhenjie Yan,^{1,2} and Dan M. Stamper-Kurn^{1,2,5,†}

¹*Department of Physics, University of California, Berkeley, California 94720*

²*Challenge Institute for Quantum Computation, University of California, Berkeley, California 94720*

³*Max-Planck-Institut für Quantenoptik, 85748 Garching, Germany*

⁴*Munich Center for Quantum Science and Technology (MCQST), 80799 Munich, Germany*

⁵*Materials Sciences Division, Lawrence Berkeley National Laboratory, Berkeley, California 94720*

ATOM PREPARATION AND STATE INITIALIZATION

Our optical tweezer array is formed by multiple beams of light at a wavelength of 808 nm generated by an acousto-optic deflector (AOD). The tweezer beams are focused through a NA = 0.5 objective to a beam waist radius ($1/e^2$ intensity) of 750 nm. The tweezer array is initially overlapped with an optical dipole trap at a wavelength of 1064 nm, containing a thermal cloud of 10^5 atoms with a temperature of 30 μ K and $1/e$ density radius of 10 μ m (2 mm) along its radial (axial) direction. The dipole trap is extinguished 10 ms after switching on the tweezer traps. The tweezers are then exposed to polarization gradient cooling light and repump light for 125 ms, reducing the atom number in each tweezer to either zero or one [S1], while the atomic fluorescence is collected through the high-NA objective (exposure time of 100 ms) to determine the tweezer occupation.

After tweezer loading and imaging, the atoms are prepared in the $F = 1$ and $F = 2$ ground state manifolds without Zeeman-state-specificity for the cavity measurements shown in Figs. 2 and 3. For initialization in the $F = 1$ ($F = 2$) manifold, the atoms are exposed to depump (repump) light resonant with the D_2 $F = 2$ ($F = 1$) \rightarrow $F' = 2$ transition for 0.75 ms (2 ms).

For the Ramsey measurements shown in Fig. 4, the atoms are prepared in the initial state $|F = 2, m_F = 0\rangle$. Under an applied bias magnetic field of 5 G, we illuminate the atoms simultaneously with π -polarized depump light and σ^\pm -polarized repump light for 1 ms. This optical pumping process results in a 90% preparation fidelity based on the contrast of Rabi oscillations observed immediately after state preparation on the $|F = 2, m_F = 0\rangle \rightarrow |F = 1, m_F = 0\rangle$ microwave transition.

CAVITY PARAMETERS

Cavity ringdown measurements yield a cavity half width at half maximum of $(2\kappa) = 2\pi \times 0.53$ MHz and a finesse of 14700 for the cavity mode at 780 nm wavelength [S2]. Using single atom scanning probe microscopy, we measured the cavity mode waist radius ($1/e^2$ intensity) to be $w_0 = 20(3)$ μ m [S3]. With a cavity length of 9.4 mm, we derive the maximum atom-cavity coupling strength for the $|F = 2, m_F = 2\rangle \rightarrow |F = 3, m_F = 3\rangle$ stretched state transition to be $g_0 = 2\pi \times 2.7$ MHz.

To facilitate detection, the optical cavity features two mirrors with asymmetric transmissivity of 3.5 and 250 ppm at the probe wavelength of 780 nm. With total loss and transmission of 430 ppm based on the measured cavity finesse, cavity photons thus enter the detection optics through the cavity's more transmissive outcoupling mirror with an efficiency of 58%. These photons are routed into an optical fiber and onto a single photon counting module (SPCM: SPCM-AQR-13) with total optical path efficiency of 65%. The quantum efficiency of the detector is 66%. Multiplying these three factors yields an overall cavity photon detection efficiency of $\eta = 25\%$.

The cavity length is tuned and stabilized by driving the cavity with narrow and tunable frequency light at a wavelength of 1560 nm, and locking the cavity so that this light is resonant with a TEM₀₁ cavity mode. The dark axis of this TEM₀₁ mode lies in the horizontal plane. The vertical height of the tweezer array is tuned so that atoms are trapped and also translated horizontally along this dark axis, minimizing their exposure to 1560-nm-wavelength light. In this manner, ac Stark shifts on the D_2 transition that would be produced by the cavity-locking light (as measured previously in Ref. [S3]) are eliminated.

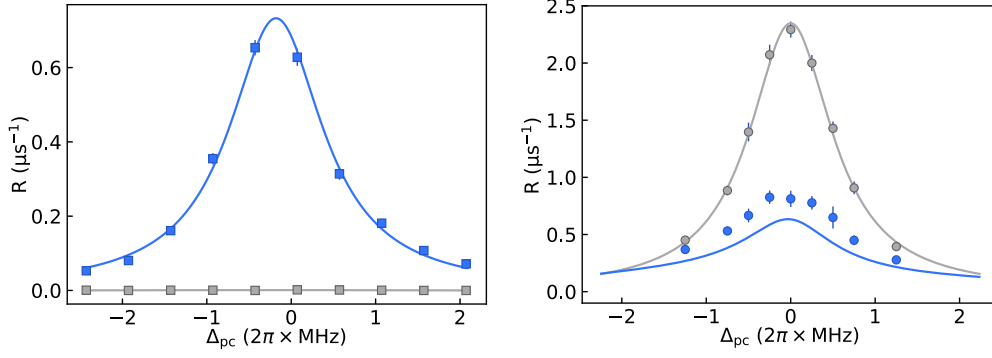


Figure S1. **Cavity fluorescence and transmission spectrum.** (a) Fluorescence photon detection rate vs. Δ_{pc} . A Lorentzian lineshape is fitted for the bright state fluorescence R_{high} (blue points). The Lorentzian fit (blue line) yields a half-linewidth of $(2\pi \times 0.68(3) \text{ MHz})$; the center of the peak is shifted from bare cavity resonance by $2\pi \times -0.15(2) \text{ MHz}$ because of the atom-induced ac Stark shift. R_{low} (gray) is measured with no atom trapped in the cavity. (b) Transmission photon detection rates vs. Δ_{pc} . R_{high} (gray points) exhibit a Lorentzian lineshape (gray curve) with fitted HWHM of $2\pi \times 0.6 \text{ MHz}$, slightly larger than κ (measured by cavity ringdown). R_{low} (blue points) is reduced to $0.35 \times R_{\text{high}}$ on resonance. Its variation with Δ_{pc} agrees qualitatively with theoretical prediction based on the Jaynes-Cummings model and including effects of spatial averaging of g^2 along the cavity axis (blue curve). The fact that R_{low} is overall higher than expected based on this theoretical prediction may be explained by ac Stark shifts of the atomic resonance line by tweezer light.

CAVITY FLUORESCENCE AND TRANSMISSION

In Fig. S1, we show the cavity photon detection rate for the fluorescence and transmission methods of detection, with the probe frequency and intensity settings described in the main text, and with variable cavity resonance frequency (indicated by Δ_{pc}). As described in the main text, with Δ_{pc} near zero, we observe a large difference between the detection rates observed with an $F = 2$ atom in the cavity (blue points) and those observed with no atom in the cavity (gray points).

The observed rates can be matched with theoretical predictions. We consider a simple model in which our system can be described by the Jaynes-Cummings Hamiltonian, with additional atomic and cavity driving terms describing the fluorescence and transmission probe light, as well as cavity photon decay at a rate 2κ and atomic excited state decay at a rate 2γ . The atom is treated as a two-level system (operated upon by the standard $\hat{\sigma}$ operators), ignoring significant dynamics of the atom within its hyperfine structure. Further, the cavity is treated as a single-mode system, ignoring the existence of two near-degenerate cavity modes of opposite polarization. In the steady state, the rate of detecting cavity photons is $R = 2\eta\kappa\langle\hat{a}^\dagger\hat{a}\rangle$, with \hat{a} being the cavity mode annihilation operator.

Considering first the fluorescence measurement, we adopt a mean-field approximation, replacing terms like $\langle\hat{a}\hat{\sigma}^+\rangle$ with $\langle\hat{a}\rangle\langle\hat{\sigma}^+\rangle$. This yields a steady-state photon field $\langle\hat{a}\rangle = ig_0\langle\hat{\sigma}^-\rangle/(\kappa - i\Delta_{\text{pc}})$ and a photon detection rate $R = 2\eta\kappa\langle\hat{a}\rangle^2 = 2\eta\kappa g_0^2\langle\hat{\sigma}^-\rangle^2/(\kappa^2 + \Delta_{\text{pc}}^2)$. At $\Delta_{\text{pc}} = 0$, a maximum cavity detection rate of $R_0 = \eta g_0^2/(4\kappa)$ is expected when $\langle\hat{\sigma}^-\rangle^2$ reaches its maximum value of $1/8$. This result agrees well with the maximum cavity scattering observed in numerical simulation of the Jaynes-Cummings master equation that we perform using QuTiP [S4]. In Fig. S1(a), we show the detected photon counts vs. Δ_{pc} fitted to a Lorentzian, which has a half-linewidth slightly larger than κ ; this extra broadening may be caused by noise in Δ_{pc} and cavity quantum electrodynamic effects.

The observed maximum cavity emission rate is not captured by the mean-field model of a two-level atom and single cavity mode. Numerical calculation of the cavity photodetection rate $R_{\parallel, \text{eff}}$ ($R_{\perp, \text{eff}}$) under probe light polarized along (perpendicular to) the cavity axis yields $R_{\parallel, \text{eff}} = 0.10R_{\text{max}}$ ($R_{\perp, \text{eff}} = 0.50R_{\text{max}}$). The fluorescence probe beams are in a lin-perp-lin molasses configuration that alternates between these two polarizations. Spatial averaging of the probe polarization and equal population of the Zeeman sublevels results in a reduction of the theoretical R_{max} by a factor of 0.28.

Next we move to the transmission measurements, where the two-level picture is more applicable because the atom is pumped to the stretched state by the circularly-polarized transmission probe light. Fig. S1(b) shows the transmission through the cavity versus Δ_{pc} in the low-saturation regime. The theoretical factor of $R_{\text{low}}/R_{\text{high}}$ vs. Δ_{pc} in the weak-drive regime is given in Ref. [S5]. Taking that result, and performing a uniform spatial average along the cavity axis, we obtain the blue curve shown in Fig. S1(b). Both this predicted and the observed R_{low} transmission line shape are broadened with respect to that of the empty cavity. The observed cavity transition R_{low} is generally higher than

the predicted value. This discrepancy is likely caused by ac Stark shift variation produced by the optical tweezer light.

In Fig. 3(c), we use Ashman’s D function [S6] to quantify the separation of the high and low cavity transmission distributions. Considering two distributions with means $\mu_{1,2}$ and standard deviations $\sigma_{1,2}$, Ashman’s D is defined as $D = |\mu_1 - \mu_2|/\sqrt{(\sigma_1^2 + \sigma_2^2)/2}$.

RAMSEY MEASUREMENT

A bias magnetic field is applied during the Ramsey sequence to lift the degeneracy of the Zeeman sublevels and confine the atom within the $m_F = 0$ subspace. The fluorescence measurement operates under a bias field of 5 G that is aligned with the propagation direction of the fluorescence probe beams, which allows for simultaneous one-dimensional sub-Doppler cooling during the measurement. We note that this field setting is different than for the fluorescence measurement characterized in Fig. 2 in the main text, for which the applied field is near zero. It is possible that the higher magnetic field setting used in this two-atom experiment increases the overall infidelity of measurement. However, this increased infidelity does not affect the main focus of the two-atom experiment, which is the characterization of additional decoherence on atom B owing to the measurement on atom A.

For the transmission measurements, the field orientation is rotated after state preparation to be aligned with the cavity axis, and the field amplitude is reduced to 2 G. This allows the atoms to be pumped into the stretched state by circularly-polarized transmission probe light during measurement. The microwave field driving the $\pi/2$ pulses has a Rabi frequency of $2\pi \times 2.1$ kHz and $2\pi \times 4.8$ kHz for the fluorescence and transmission measurements, respectively. This difference is due to field projection along different quantization axes.

To quantify the decoherence of the out-of-cavity atom induced by the local probe light, which is on for 2τ , and the local repump light, which is on for τ_{rp} , we measure the normalized Ramsey contrast \tilde{C} of atom B after measuring atom A with various τ and τ_{rp} larger than the optimal value, as shown in Fig. S2. The measured results are fitted by a function

$$\tilde{C}(\tau, \tau_{\text{rp}}) = \exp[-(\lambda_1\tau + \lambda_2\tau_{\text{rp}})], \quad (\text{S1})$$

where λ_1 and λ_2 describe decoherence rates caused by the probe and repump light, respectively. This method gives a lower bound of $\tilde{C} > 97.4\%$ with 84% confidence interval for fluorescence detection with $(\tau, \tau_{\text{rp}}) = (25 \mu\text{s}, 5 \mu\text{s})$ and atom distance $d = 34.5 \mu\text{m}$, as well as $\tilde{C} > 97.0\%$ for transmission detection with $(\tau, \tau_{\text{rp}}) = (50 \mu\text{s}, 5 \mu\text{s})$ and atom distance $d = 46.0 \mu\text{m}$ —in both cases well away from the probe beam waist.

Let us assume that decoherence of atom B owing to the measurement on atom A is dominantly caused by atom B’s direct exposure to probe light (i.e. not the secondary exposure to light scattered by atom A), and that a single scattered photon completely decoheres atom B. We can then estimate the decoherence rate $\lambda_1 = \mathcal{R}e^{-d^2/2w^2}$ where \mathcal{R} is the scattering rate from an $F = 2$ atom at the location of maximum intensity of the probe beam ($d = 0$), and w is the $1/e^2$ -intensity probe beam waist radius. Values of \mathcal{R} are determined already by the cavity emission observed when measuring a single tweezer-trapped atoms; for the data of Fig. 4(c) (main text), we take these as $\mathcal{R} = 4.33 \mu\text{s}^{-1}$ ($2.34 \mu\text{s}^{-1}$) for fluorescence (transmission) measurements. In the case of fluorescence probing, the beam waists of the two counter-propagating probe beams differ: The downward-going beam (focused by the high-NA lens) has a beam waist around $3.3 \mu\text{m}$, while the upward-going beam has a beam waist around $13 \mu\text{m}$. For simplicity, for the above estimate, we simply use $w = 13 \mu\text{m}$. In the case of transmission probing, we set $w = w_0$, matching the cavity mode waist. The reductions in normalized contrast predicted by this treatment are shown as dashed (fluorescence) and dotted (transmission) lines in Fig. 4(c).

SPAM ERROR ANALYSIS

In Figs. 2 and 3 and Table 1, the reported infidelity on each state is the probability of the measurement outcome falling outside of the correct quadrant, calculated directly from the observed SPAM error over many experimental repetitions, and based on Bayesian probability theory.

Here, we describe how we distinguish state preparation error from measurement error. We focus our discussion on fluorescence detection. We describe a tweezed atom in the $F = 2$ manifold as the bright state, and the other tweezer state possibilities (empty tweezer, or tweezer with an atom in the $F = 1$ manifold) as dark states.

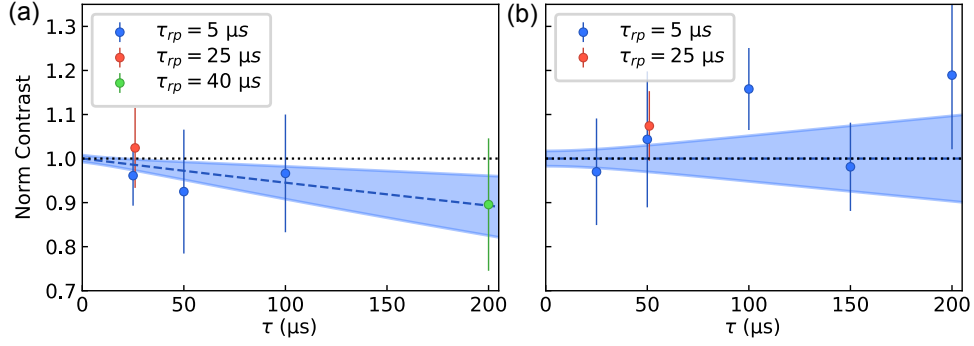


Figure S2. **Normalized Ramsey contrast** measured for atom B with various probe interval τ and repump time τ_{rp} for atom A measurement. (a) Fluorescence measurement at a distance of $d = 34.5 \mu\text{m}$. (b) Transmission measurement at a distance of $d = 46.0 \mu\text{m}$. The blue dashed line indicates the fitted decoherence with $\tau_{rp} = 5 \mu\text{s}$, while the blue shaded area indicates the uncertainty of the fit.

State measurement error is the sum of single interval measurement (SIM) errors in each interval: $\epsilon_{F=2} = P^-$; $\epsilon_{F=1} = P^+ + P^-$; $\epsilon_{\text{empty}} = 2P^+$. Here we define positive (negative) SIM errors $P^+(P^-)$ as the probability of having first-interval photon count above (below) the bimodal threshold for a dark (bright) state atom. We set the threshold between 0 and 1 photons (which we denote as $n_{\text{th}} = 0$) for $\tau \leq 15 \mu\text{s}$ and between 1 and 2 photons ($n_{\text{th}} = 1$) for $\tau > 15 \mu\text{s}$, so that $\max(P^+, P^-)$ is minimized.

The dark state photon counts follow a Poisson process of rate $R_{\text{dark}} \simeq 0.4 \text{ ms}^{-1}$ (the dark count rate of the SPCM). Using the cumulative distribution function (CDF) of a Poisson distribution $Q(n_{\text{th}}, \lambda) = e^{-\lambda} \sum_{m=0}^{n_{\text{th}}} \frac{\lambda^m}{m!}$, we can write the positive SIM error as

$$P^+ = 1 - Q(n_{\text{th}}, R_{\text{dark}}\tau) \quad (\text{S2})$$

The bright state photon count deviates from the Poisson distribution in two ways. Firstly, Zeeman sampling and spatial sampling of g randomize the scattering rate $R \rightarrow \tilde{R}$, broadening the observed photon-count distribution above the Poisson limit by a Fano factor \mathcal{F} observed to be 1.7 (2.2) for fluorescence (transmission) detection. Secondly, the $F = 2$ atom can either off-resonantly depump into the $F = 1$ manifold or be heated out of the tweezer trap mid-interval, resulting in a randomized fluorescence time $\tau \rightarrow \tilde{t}$ with average lifetime T . A state-jump error occurs if the SPCM has not yet counted an above-threshold number of photons before the atom goes dark. The Poissonian CDF $\tilde{P}^-(\tilde{R}, \tilde{t}) = Q(n_{\text{th}}, \tilde{R}\tilde{t})$ also becomes a random variable, and we calculate the negative SIM error as its expectation value:

$$P^- = \mathbb{E}(\tilde{P}^-(\tilde{R}, \tilde{t})) = \int_0^\tau \rho_t(\tilde{t}) d\tilde{t} \int_0^\infty \rho_R(\tilde{R}) d\tilde{R} Q(n_{\text{th}}, \tilde{R}\tilde{t}), \quad (\text{S3})$$

where $\rho_R(\tilde{R}) \propto \text{Exp}\left(-\frac{(\tilde{R}-R_{\text{max}})^2}{2(\mathcal{F}-1)R_{\text{max}}}\right)$ and $\rho_t(\tilde{t}) = \frac{1}{T}e^{-\tilde{t}/T} + e^{-\tau/T}\delta(\tilde{t}-\tau)$. As $\tau \rightarrow \infty$, while random sampling only slows down the speed at which P^- asymptotes to 0, state-jump error causes P^- to reach a minimum of $P_{\text{sj}}^- = (1 + 2R_{\text{max}}T)/(1 + R_{\text{max}}T)^2 = 0.2\%$, where $T = 1.6 \text{ ms}$ is the measured bright state lifetime at $\Delta_{\text{pc}} = 2\pi \times (-10) \text{ MHz}$. This is lower than the measured $F = 2$ infidelity in the long probe limit ($\sim 0.5\%$) as shown Fig 2d. We take the remaining unaccounted error of 0.3% to be state preparation infidelity. For this setting, therefore, the state-preparation error and measurement error are roughly equal in magnitude, as stated in the main text. By fixing the values above for R_{dark} , \mathcal{F} , T and the state-preparation error, we obtain the predicted SPAM infidelities plotted as lines in Fig. 2(d).

For a larger detuning $\Delta_{\text{pc}} = 2\pi \times (-20) \text{ MHz}$, we increase the fluorescence beam intensity by roughly a factor of 4 to reach the same cavity scattering rate R_{high} . At this intensity, we observe a shorter state lifetime of $T \simeq 0.4 \text{ ms}$, corresponding to a state-jump error of $P_{\text{sj}}^- \simeq 0.8\%$ and thus increasing the observed infidelity in the long probe limit to 1.1%.

Similar analysis can be carried out for transmission detection, where depump error will cause P^- to increase with probe time at long probe times, as shown by the lines showing the predicted SPAM infidelities in Fig. 3(d).

* These authors contributed equally to this work.

† dmsk@berkeley.edu

- [S1] N. Schlosser, G. Reymond, I. Protsenko, and P. Grangier, Sub-Poissonian Loading of Single Atoms in a Microscopic Dipole Trap, *Nature* **411**, 1024 (2001).
- [S2] J. A. Gerber, *Cavity Quantum Electrodynamics with a Locally Addressable Quantum Gas*, Ph.D. thesis, University of California Berkeley (2020).
- [S3] E. Deist, J. A. Gerber, Y.-H. Lu, J. Zeiher, and D. M. Stamper-Kurn, Superresolution microscopy of optical fields using tweezer-trapped single atoms, *Phys. Rev. Lett.* **128**, 083201 (2022).
- [S4] J. R. Johansson, P. D. Nation, and F. Nori, QuTiP 2: A Python framework for the dynamics of open quantum systems, *Comput. Phys. Commun.* **184**, 1234 (2013).
- [S5] J. Bochmann, M. Mücke, C. Guhl, S. Ritter, G. Rempe, and D. L. Moehring, Lossless State Detection of Single Neutral Atoms, *Phys. Rev. Lett.* **104**, 203601 (2010).
- [S6] K. A. Ashman, C. M. Bird, and S. E. Zepf, Detecting bimodality in astronomical datasets, *Astron. J.* **108**, 2348 (1994).